Numerical Simulation and Validation of NACA0012 Airfoil to Predict Its Performance During the Stalling Condition

Dishant Sharma and Rahul Goyal

1 Introduction

Current energy demand, decreasing fossil fuel reserves, and stringent environmental restrictions all contribute to the widespread adoption of renewable energy sources such as wind and solar. The most effective method for harnessing wind energy is the wind turbine. The advancement of vertical axis wind turbines (VAWTs) is crucial to the future of wind power because of its viability in low-wind environments, especially in urban areas [1–4]. VAWTs have advantages over horizontal axis wind turbines (HAWTs) in omnidirectional behaviour, higher scalability, better performance in chaotic, unstable, and turbulent flow conditions, lower maintenance, and higher overall efficiency for the entire wind farm [5–7]. In contrast, due to instability in terms of flow disturbances around the blade, rapid and cyclic changes in the angle of attack introduce dynamic stall.

The complicated chain of events known as dynamic stall occurs when an airfoil is subjected to rapid changes in angle of attack that go beyond the situation known as static stall. In the case of a two-dimensional flow, the dynamic stall processes during blade pitching involve the formation, growth, and shedding of the vortex structure. Qualitative characteristics of dynamic stall include the gradual reversal of the boundary layer from the trailing edge, the breakdown of the flow due to the bursting of laminar bubbles, and the emergence of a turbulent separation towards the leading edge. One common unwanted phenomenon in VAWTs is the appearance of a wake on the blade [8]. Downstream wind turbines experience an increase in aerodynamic loads due to the intense turbulent wake flow's influence on the development of dynamic stall characteristics [9]. Laneville and Vittecoq reported that for tip speed ratio (TSR, λ) less than or equal to 4, the dynamic stall phenomenon dominates for VAWTs [10]. As λ values fall below 4, the dynamic stall changes from a light to a

D. Sharma · R. Goyal (✉)
Department of Energy Science and Engineering, IIT Delhi, New Delhi 110016, India
e-mail: rahulgoyal@dese.iitd.ac.in

K. M. Singh et al. (eds.), *Fluid Mechanics and Fluid Power, Volume 3*, Lecture Notes in Mechanical Engineering, https://doi.org/10.1007/978-981-99-6343-0_13

deep stall. The deep dynamic stall had four main stages: attached flow at a lower angle of attack (AoA), formation of leading edge vortex (LEV), shedding of LEV from the suction surface of the airfoil, and reattachment of the flow [11, 12]. This investigation on the dependence of λ on stall formation has uncovered a problem that will require further investigation. The formation and growth of LEV on suction side of the airfoil increases lift, and the shed off of this vortex from the surface of the airfoil causes transitory variations in the continuous torque delivery, lift, and drag performance metrics, resulting in decreased turbine power. It poses a severe problem to VAWTs since vibrations and induced noise reduce stability and efficiency [13].

The primary focus of the current work is to conduct a rigorous quantitative investigation of the performance characteristics, boundary layer flow features on the airfoil, lift and drag fluctuations, and angle of attack changes for a single-bladed rotor system. The dynamic stall phenomenon, which affects turbine efficiency, is given special attention. The current simulation runs at a moderate Reynolds number with a NACA0012 blade profile based on one of the Lee and Gerontakos [14] experiments' oscillating cases during the deep stall condition, where the AoA varies as $\alpha(t) = 10^\circ + 15^\circ \sin \omega t$ and the reduced frequency is 0.1. This case merited choice because it involved an investigation into deep stall regime conditions and yielded higher performance outcomes in comparison to other situations found in the literature [14]. The Lee and Gerontakos [14] experimental work serve as a basis for this numerical work's validity, and the observations drawn from the results are covered in the sections that follow. The work comprises of grid independency test (GIT), then followed by validation of numerical results with aforementioned experimental work. It was observed that the results obtained are in good agreement with experimental for all critical points except one. Details of which have been explained in the results section. Additionally, velocity vectors around the airfoil have been obtained to offer a visual depiction of the described underlying flow physics.

2 Numerical Methodology

The experimental work by Lee and Gerontakos [14] was performed numerically using commercial software ANSYS [15]. The available numerical model in the literature was re-developed using ANSYS-ICEM and ANSYS-Fluent solver. The experimental results of the literature [14] were used to validate the current results. The two-dimensional study that was conducted on the NACA0012 airfoil of 150 mm chord length consists of a computational domain, which was separated into two zones: the size of the stationary zone was $35D \times 20D$, and the size of the rotational zone was $1.5D$ for the current scenario, as shown in geometry Fig. 1. Here, D is typically the diameter of the turbine, but due to the single-blade rotor case, D is the chord length of the airfoil. The distance between the inlet of the domain to the rotor centre was $10D$, which is kept to avoid errors of overestimation [16]. In order to maintain the uniform pressure coefficient at the outlet, a distance of $25D$ was considered from the rotor centre. The domain width was calculated considering a less than 5% blockage

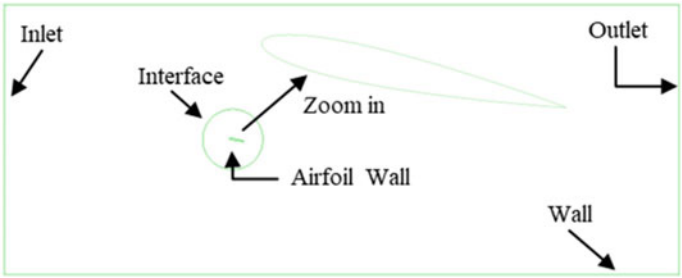

Fig. 1 Computational domain geometry of the NACA0012 airfoil comprises both fixed and rotating zones

ratio. The diameter of the rotating core was $1.5D$ for the present case to get a better grid generation capability. The dimensions of the flow domain were determined after taking into account the impacts of blockage ratio and the uncertainty caused by the boundary wall. A non-conformal interface with sliding mesh technique between the fixed and rotating domains allows the single-bladed rotor to rotate.

The moderate mainstream Reynolds numbers for the current cases are in the range of 100,000–150,000. The experimental static stall angle of the symmetric NACA0012 airfoil is around 13°.

$$\mathrm{Re} = \frac{\rho V C}{\mu}. \tag{1}$$

The local coefficient of friction ($C_{f}\prime$) calculated using the empirical relation given by Eq. (2) [17]

$$C_{f}\prime = (2\log \mathrm{Re} - 0.65)^{-2.3}. \tag{2}$$

Equation (3) is used to compute the wall shear stress (τ_{ω})

$$\tau_{w} = 0.5 C_{f}\prime \rho V^{2}. \tag{3}$$

The frictional velocity can be computed as

$$u_{t} = \left(\frac{\tau_{w}}{\rho}\right)^{0.5}. \tag{4}$$

An inflation with a first layer thickness of 0.01585 mm is given on the edge of the airfoil, ensuring precision at airfoil's boundary zone. Equation (4) is used to determine the blade's first layer thickness [18]

$$y+ = \frac{\rho u_{t} y}{\mu}. \tag{5}$$

ICEM grid generation software [15] was used to construct the grid for the entire domain. To accurately resolve the viscous sublayer and visualize the flow around the airfoil wall, the *y*+ is taken into account by refining the grid near the surface and keeping the value less than 1, which can be depicted numerically also as a range along the chord length as shown in Fig. 2b. The growth rate of 1.2 for the boundary layer mesh was considered. Turbulence models were also chosen depending on the *y*+ values. Grid-dependent investigations were conducted to determine the optimal grid size for the computing domain. Table 1 of the result section displays the findings acquired from the grid-dependent investigations for one of the critical angles. The mesh matrix for the present case, like skewness, orthogonal quality, aspect ratio and overall quality are in good agreement.

The transient, incompressible, two-dimensional flow condition with URANS equations and Reynolds stresses was modelled using a 5-equation turbulent model with 1-equation of intermittency. The current study employed the SAS-based SST *k*-*ω* turbulence model. The SST-SAS turbulence model exhibits scale adaptivity in

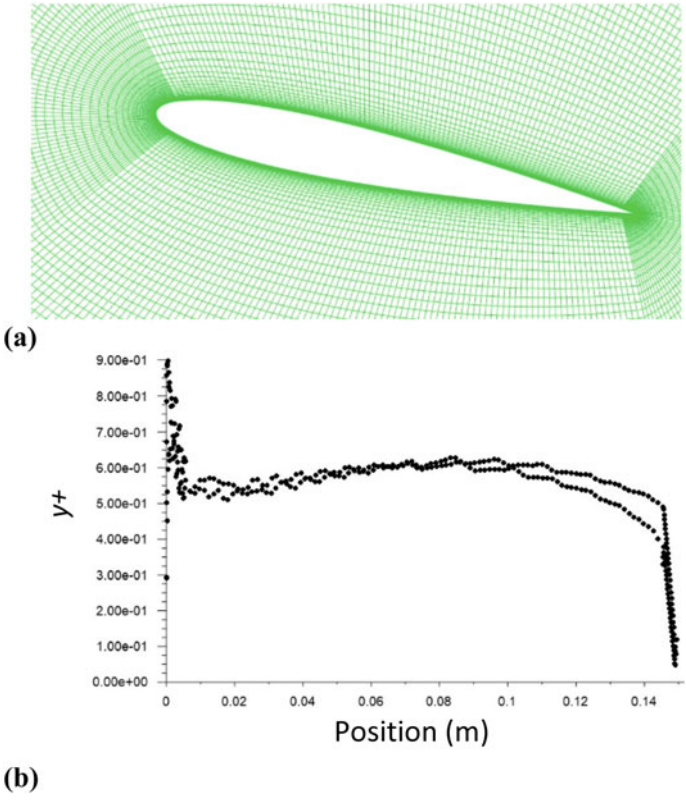

Fig. 2 **a** Close view of the structured mesh near to the airfoil and **b** variation of the wall ***y*+** of the NACA0012 airfoil along the chord length position

contrast to conventional RANS models. It can dynamically resolve turbulent structures in an unsteady flow field while keeping URANS capability in steady flow regions. This can be achieved by including the von Karman length scale into the turbulence scale equation, which can be found in the reference [15].

For computation, the density of air and viscosity is taken as 1.225 kg/m^3 and 1.7894×10^{-5}, respectively. In the cell zone condition, the rotating and stationary mesh motion is provided with 18.535 rad/s rotational velocity. The boundary conditions consist of inlet as velocity type having 13.15 m/s magnitude and direction in the x axis. The turbulence intensity is kept 0.08 and turbulent length scale as 0.0105. The outlet boundary condition is pressure outlet and walls as no slip and stationary. For momentum, the spatial discretization technique is Bounded Central Differencing, while for other functions, it is QUICK. For the pressure–velocity coupling, the SIMPLE scheme is employed, and the transient formulation is done using the Bounded second-order implicit. All of the equations should meet the convergence criterion of less than 10^{-4}. To obtain reliable findings, the time step calculation needs to be carried out in consideration of CFL criteria. The time step size of 1.88×10^{-5} is computed considering the courant number less than unity and the rotational velocity of the rotating domain. The CFL number obtained for the present case using Eq. (6) is 0.36, ensuring grid and numerical stability [19]:

$$\mathrm{CFL} = V \frac{\Delta t}{\Delta x}. \tag{6}$$

After ten revolutions, the data for the current case was obtained, and the findings of an additional four revolutions were analysed.

3 Results and Discussion

3.1 Grid Independence Test

The grid independent test was carried out for the present case. Three grids were generated and conducted the simulation for each one. Table 1 displays the findings that were acquired from the grid independent investigations for one of the critical angles (21°). Based on the observed values of lift and moment coefficient, Grid 2 is chosen for the remainder of the study due to the insignificant change in lift and moment coefficient values and the lower computational cost and time requirements.

Table 1 Details of the computational grid and its performance characteristics

Case	No. of cells	Moment coefficient (C_m)	Lift coefficient (C_L)
Grid I	74772	0.59	1.83
Grid II	149212	0.61	1.96
Grid III	301492	0.60	1.97

3.2 Validation of Numerical Model

The experimental findings of Lee and Gerontakos were used to validate the current numerical work and compared with the SAS-SST turbulence model results. The anticipated lift coefficient for the critical angle of attacks was plotted in Fig. 3a. The results demonstrate good agreement with the experimental values as stated in Table 2. The current numerical results showed good agreement on comparing with the experimental and numerical results of the literature [14, 20, 21]. The coefficients of lift obtained from this study for various angles of attack are close to the experimental values. The modelling predicts the onset of static stall around a 12° AoA, which is consistent with experiment. An increase in angle of attack up to 24° results in an increase in coefficient of lift. The onset of dynamic stall is noted around a 24° AoA. As the AoA reaches to 25° during upward motion, a reverse downward movement of the airfoil up to 0° AoA was commenced, resulting in a fall in predicted lift coefficient in accordance with experiment. It is important to note that the agreement to experiment failed during the transition from 24.9° to 24.5°. Although the experiment demonstrated an increase in lift coefficient during this event in an otherwise decreasing trend, simulation was unable to detect this rise and instead predicted a drop. However, the current results have significant improvement in prediction of aerodynamic forces compared to the numerical work of Rahman et al. [20] due to the better turbulence model, the structured mesh, the number of grid elements, the time step size, and the number of revolutions. Singh and Páscoa's [21] results are quite comparable to the current case, but the percentage of error is reduced for 7 critical points. This may be due to optimum geometry parameter selection and number of revolutions.

In the upward motion of the airfoil, the predicted values of the lift and drag coefficients by the SST-SAS turbulence model were in good agreement with the experimental findings. During the downward movement, secondary vortex formation causes an increase in lift for a small range of AoA that the current model unable to predict.

However, it is able to capture and better anticipate the events of post-stall, reattachment, and fully attached flow to the airfoil, as depicted in Fig. 3a. The current model manages to predict closely the drag coefficient for the onset of transition event at 12° AoA but overestimates the drag coefficient values for the event turbulence separation $\alpha \approx 17°$ and near to stall $\alpha = 24°$, as illustrated in Fig. 3b.

Figure 4 presents a comparison of the performance in terms of lift to drag coefficient ratio with the change in the angle of attack for upward motion case. The

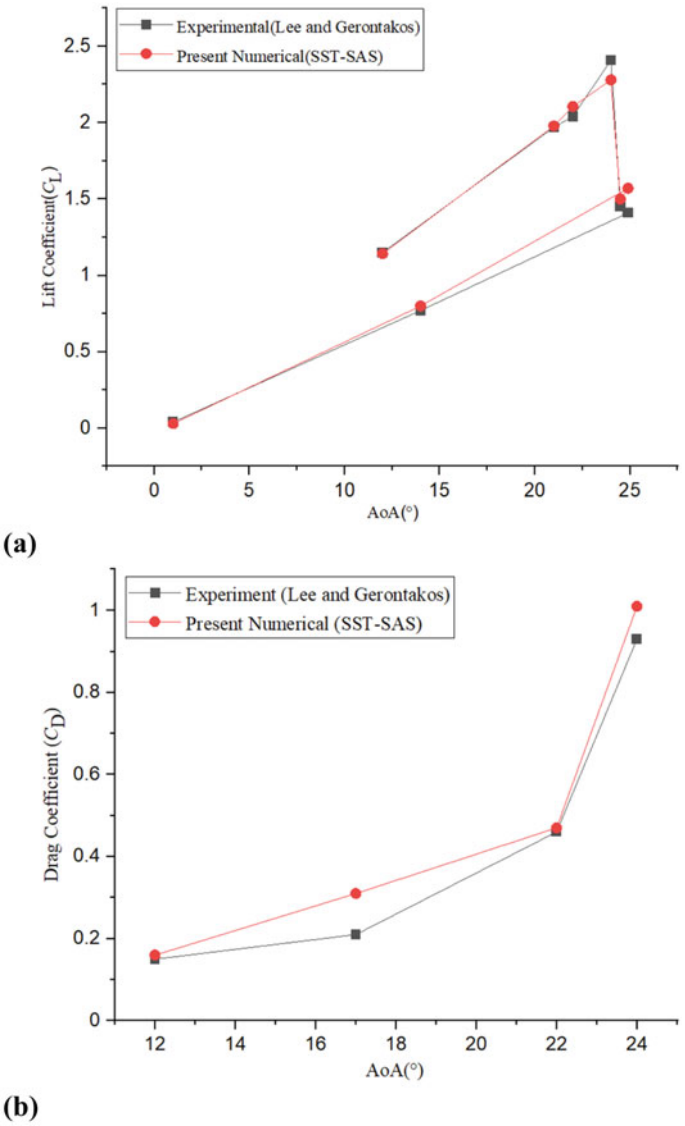

Fig. 3 **a** Variation of C_L with AoA and **b** variation of C_D with AoA of the NACA0012 airfoil

numerical values that are anticipated to occur during the pre-stall and dynamic stall conditions are underestimated up to 21°. This is because the drag coefficient values were overestimated, as can be seen in Fig. 3b. In comparison with the numerical results of Singh and Páscoa's [21], the present C_L/C_D numerical results demonstrate good agreement with the experiment at $\alpha \geq 21°$. This quantitative comparison of lift, drag, and lift to drag coefficients with experiment and numerical references [14,

Table 2 Comparing the experimental results of Lee and Gerontakos [14] at critical points with the current numerically calculated lift coefficient

AoA	Experimental	Present numerical	Error (%)
12	1.15	1.145	0.43
21	1.97	1.96	0.5
22	2.04	2.09	− 2.45
24	2.41	2.25	6.63
24.9	1.41	1.45	− 2.83
24.5	1.45	1.42	2.06
14	0.77	0.74	3.89
1	0.04	0.03	25

20, 21] demonstrates good agreement and the capabilities of SST-SAS turbulence model. Utilizing more advanced turbulence models in future research, such as LES, will allow more accurate prediction of important events such as turbulence separation, near-stall conditions, and the formation of secondary vortices.

The aforementioned performance matrices for the current case can be explained further with the velocity vector fields as shown in Fig. 5. The important observations of the flow physics involved for the pitching airfoil in deep dynamic stall condition are as follows:

For $\alpha < 12°$: Over the entire range of the AoA, the flow continues to be laminar and adhered to the suction surface of the airfoil. Figure 5a shows flow detachment

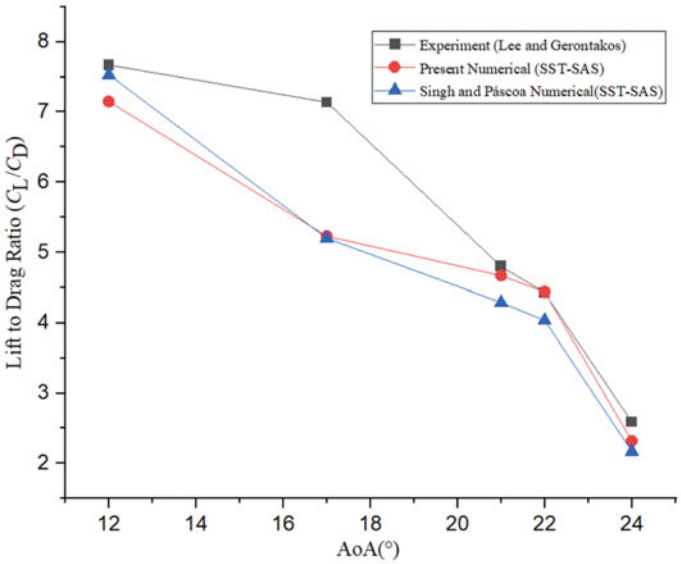

Fig. 4 Performance variation of C_L/C_D with AoA of the single-bladed rotor system

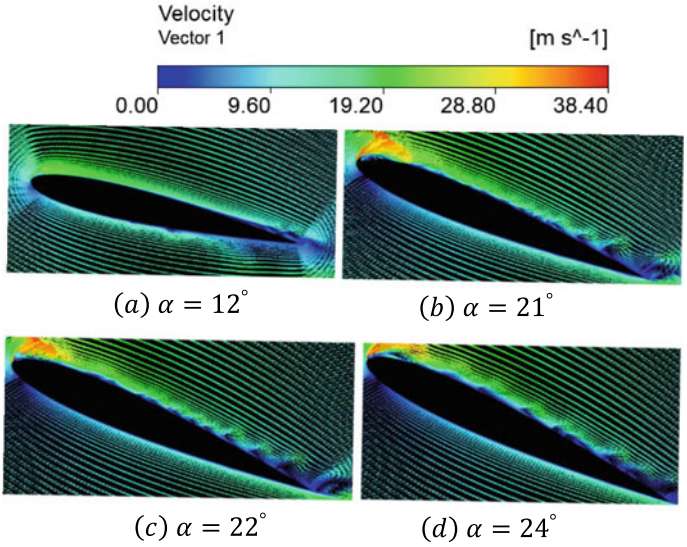

Fig. 5 Velocity vector plots during the upward motion of the airfoil for critical AoA

near the end of the trailing edge, which was previously confirmed experimentally by Lee and Gerontakos [14].

For $12° \leq \alpha \leq 21°$: The development of flow transition and reversal is observed with the increase in AoA. Flow reversal from trailing edge propagates towards the leading edge, as shown in Fig. 5b.

For $21° \leq \alpha < 25°$: With the increase in AoA, turbulent boundary layer breakdown can be visualized due to formation of dynamic stall vortex and adverse pressure gradient as shown in Fig. 5c, d. It rapidly increases the lift and drag coefficients which can be seen in Fig. 3a, b.

4 Conclusions

The current work presents an understanding of the flow dynamics, effect of change in angle of attack on aerodynamic performance in terms of lift and drag fluctuations for a single-bladed rotor. A rigorous quantitative investigation of the performance characteristics, boundary layer features, and the dynamic stall phenomenon on the airfoil which affects turbine efficiency is given special attention. For validating the experimental results and to visualize the vortex formation, Scale Adaptive Simulation is incorporated with SST k-ω turbulence model. The current numerical results of aerodynamic forces exhibit good agreement with the experiment for pre-stall events when compared to the numerical references [14, 20, 21]. Lift coefficient values are obtained with a percentage error of less than 4% for six critical AoA's out of eight.

The remaining two AoA's (24° during upward motion and 1° during downward motion) are observed with a percentage error of 6.63 and 25%. The flow reversal and progression depicted by velocity vectors aids in visualizing the crucial turbulent boundary layer events that occur over the airfoil. The generation, development, accumulation, and shedding of vortex structures from the suction surface of an airfoil are clearly observed using velocity vectors. It can be seen that the flow reversal started at around 12° AoA near to the trailing edge due to adverse pressure gradient. It is also observed from the velocity vectors that the flow reversal propagates from trailing edge to leading edge as the AoA increases but the boundary layer remains attached to the airfoil up to 21° AoA. Further increase in AoA results in turbulent boundary layer breakdown and formation of LEV, which further develops and convects over the suction surface of the airfoil, resulting in a rapid increase in lift. The shedding of vortex after further increment in AoA results in abrupt aerodynamic losses yielding a compromised airfoil performance. An important subject of application of the present analysis is the VAWT which relies on multiple airfoils for development of lift and consequent rotational shaft power. The analysis thereby serves to be a tool in performance prediction of VAWTs and may be used to identify, assess, and improve in future scope the optimal working conditions of these turbines.

Nomenclature

AoA(α)	Angle of attack (°)
CFL	Courant–Friedrichs–Lewy [–]
LEV	Leading edge vortex [–]
NACA	National Advisory Committee for Aeronautics [–]
SAS	Scale Adaptive Simulation [–]
SST	Shear stress transport [–]
SIMPLE	Semi-Implicit Method for Pressure Linked Equations [–]
QUICK	Quadratic Upstream Interpolation for Convective Kinematics
Re	Reynolds number
c	Airfoil chord [m]
C_L	Lift coefficient [–]
C_D	Drag coefficient [–]
C_m	Moment coefficient [–]
$C_\mathrm{f}\prime$	Skin friction coefficient [–]
δ	Boundary layer thickness [mm]
λ	Tip speed ratio [–]
ρ	Density of air [kg/m^3]
D	Turbine diameter [m]
V	Free stream velocity [m s^{-1}]
μ	Dynamic viscosity [kg m^{-1} s^{-1}]
k	Turbulence kinetic energy [m^{2}s^{-2}]
ω	Specific turbulence dissipation rate [s^{-1}]

θ	Azimuthal angle (°)
τ_ω	Wall shear stress [N m^{-2}]
μ_t	Frictional velocity [m s^{-1}]
$y+$	Non-dimensional distance [–]
y	First layer thickness [mm]
κ	Reduced frequency [–]

References

1. Simic Z, Havelka JG, Bozicevic VM (2013) Small wind turbines—a unique segment of the wind power market. Renew Energy 50:1027–1036. https://doi.org/10.1016/j.renene.2012.08.038
2. Douak M, Aouachria Z, Rabehi R, Allam N (2018) Wind energy systems: Analysis of the self-starting physics of vertical axis wind turbine. Renew Sustain Energy Rev 81:1602–1610. https://doi.org/10.1016/j.rser.2017.05.238
3. Kant A (2020) India 2020—energy policy review. https://doi.org/10.1007/bf03404634
4. Lee J, Zhao F (2021) Global wind report 2021
5. Paraschivoiu I (2002) Wind turbine design: with emphasis on Darrieus concept
6. Islam MR, Mekhilef S, Saidur R (2013) Progress and recent trends of wind energy technology. Renew Sustain Energy Rev 21:456–468. https://doi.org/10.1016/j.rser.2013.01.007
7. Mohamed MH (2014) Aero-acoustics noise evaluation of H-rotor Darrieus wind turbines. Energy 65:596–604. https://doi.org/10.1016/j.energy.2013.11.031
8. Sanderse B (2009) Aerodynamics of wind turbine wakes (ECN-E--09-016). Energy Res Cent Netherlands. http://resolver.tudelft.nl/uuid:9f4dd67d-5fe2-4e86-b2b3-497852de4ea7
9. Leu TS, Yu JM, Hu CC, Miau JJ, Liang SY, Li JY et al (2012) Experimental study of free stream turbulence effects on dynamic stall of pitching airfoil by using particle image velocimetry. Appl Mech Mater 225:103–108. https://doi.org/10.4028/www.scientific.net/AMM.225.103
10. Laneville A, Vittecoq P (1986) Dynamic stall: the case of the vertical axis wind turbine. J Sol Energy Eng Trans ASME 108:140–145. https://doi.org/10.1115/1.3268081
11. Li S, Zhang L, Yang K, Xu J, Li X (2018) Aerodynamic performance of wind turbine airfoil DU 91-W2-250 under dynamic stall. Appl Sci 2018:8. https://doi.org/10.3390/app8071111
12. Jain S, Saha UK (2020) On the influence of blade thickness-to-chord ratio on dynamic stall phenomenon in H-type Darrieus wind rotors. Energy Convers Manag 2020:218. https://doi.org/10.1016/j.enconman.2020.113024
13. Crespo A, Hernández J (1996) Turbulence characteristics in wind-turbine wakes. J Wind Eng Ind Aerodyn 61:71–85. https://doi.org/10.1016/0167-6105(95)00033-X
14. Lee T, Gerontakos P (2004) Investigation of flow over an oscillating airfoil. J Fluid Mech 512:313–341. https://doi.org/10.1017/S0022112004009851
15. ANSYS Inc. (2015) ANSYS fluent theory guide 12.0
16. Rezaeiha A, Kalkman I, Blocken B (2017) CFD simulation of a vertical axis wind turbine operating at a moderate tip speed ratio: guidelines for minimum domain size and azimuthal increment. Renew Energy 107:373–385. https://doi.org/10.1016/J.RENENE.2017.02.006
17. Schlichting H, Kestin J (1961) Boundary layer theory
18. Sharma S, Sharma RK (2016) Performance improvement of Savonius rotor using multiple quarter blades—a CFD investigation. Energy Convers Manag 127:43–54. https://doi.org/10.1016/J.ENCONMAN.2016.08.087
19. Trivellato F, Raciti CM (2014) On the Courant–Friedrichs–Lewy criterion of rotating grids in 2D vertical-axis wind turbine analysis. Renew Energy 62:53–62. https://doi.org/10.1016/J.RENENE.2013.06.022

20. Hakim A, Rahman A, Ahmad N, Mohd RN, Lazim TM, Mansor S (2017) Aerodynamics of harmonically oscillating aerofoil at low Reynolds number. J Aerosp Technol Manag 9:83–90. https://doi.org/10.5028/jatm.v9i1.610
21. Singh K, Páscoa JC (2019) Numerical modeling of stall and poststall events of a single pitching blade of a cycloidal rotor. J Fluids Eng Trans ASME 2019:141. https://doi.org/10.1115/1.4040302/367361